Journal of
Materials Chemistry C

Materials for optical, magnetic and electronic devices

Accepted Manuscript

This article can be cited before page numbers have been issued, to do this please use: T. Cheng, Z. Liu and Z. Liu, *J. Mater. Chem. C*, 2020, DOI: 10.1039/D0TC03253K.

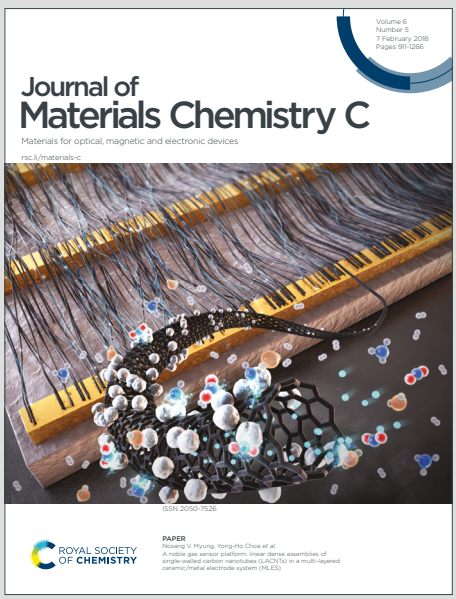

ROYAL SOCIETY OF CHEMISTRY

rsc.li/materials-c

View Article Online
DOI: 10.1039/D0TC03253K

ARTICLE

High elastic moduli, controllable bandgap and extraordinary carrier mobility in single-layer diamond

Received 00th January 20xx,
Accepted 00th January 20xx

DOI: 10.1039/x0xx00000x

Ting Cheng, [a,c] Zhongfan Liu, [a,b,c] and Zhirong Liu [a,b,*]

Very recently, the fluorinated single-layer diamond (denoted as diamane) was first successfully prepared from the conversion of bilayer graphene in a mild way by chemical vapor deposition approach, which is stable at ambient atmosphere. Herein, we performed in-depth first-principle calculations on fluorinated and hydrogenated diamane. Our calculations reveal that the fluorinated diamane is an ultrathin material with a direct-wide bandgap at Γ-point, which is 3.86 eV larger than hydrogenated diamane using the G_0W_0 method. Such bandgap could be effectively modulated by external strains or fluorine vacancy defects. Besides, their elastic moduli are comparable to graphene and are higher than most other 2D materials. The ideal tensile strength is dictated by soft-mode phonon instability under uniaxial tension and elastic instability under biaxial strain. Most surprising, we found that the calculated electron mobility (2732 $cm^2V^{-1}s^{-1}$) and hole mobility (1565 $cm^2V^{-1}s^{-1}$) in these two diamond-like monolayers are superior over those of III-V semiconductor compounds. Finally, the Raman-active phonons frequencies were characterized to serve as the fingerprint for experimentally obtained high-quality diamane. These features will boost a great potential for future applications in nano-optics, nanoelectronics, and nano-electromechanical systems.

1 Introduction

Graphene, a single-atom-thick two-dimensional (2D) material composed of sp^2 carbon atoms, has attracted enormous attention due to its high mechanical strength, thermal and electrical conductivities, and optical transparency[1-4]. Within the last ten years, more and more new 2D materials of novel physical and chemical properties were successively discovered and studied[5-7]. Nevertheless, the successful synthesis of large-scale single-crystal 2D films toward ultimate applications is yet very challenging, so graphene is still the most promising 2D material nowadays since it could be prepared into the sub-meter-size single crystal as well as layers controllable[8-11]. Besides, the carbon element is much cheaper and richer than most others. Another well-known carbon allotrope, diamond, also possessing high mechanical hardness and thermal conductivity but with sp^3 bonding hybridization compared to graphene. More importantly, the preparation of diamond is harder and more expensive, usually requiring rigid conditions, e.g., high temperature (1400-3300K) and very high pressure (5-10GPa)[12-13].

Continuously effects were made to convert the more available multilayer graphene into the ultrathin diamond film (referred to as diamane) in a mild way via designed surface-functionalization with elements such as oxygen, hydrogen, or fluorine[14-18]. Theoretical calculations suggested that such a phase transition process is thermodynamically feasible[18]. Among the surface-functional groups, F atom is much easier functionalized than hydrogenation according to the electronegativities of carbon, fluorine, and hydrogen, and has been designed to introduce in chemical vapor deposition (CVD) experiments to greatly shorten the growth time of graphene[19-20]. Very recently, Bakharev *et al*. first successfully synthesized the fluorinated single-layer diamond from bilayer graphene on CuNi (111) substrate by using XeF_2 vapor as a source of fluorine and such diamane is stable at ambient atmosphere[21]. Raeisi *et al*. explored the underlying mechanisms resulting in effects of functional groups on the thermal conductivity of diamane[22]. It is wondering whether the diamane possesses high mechanical strength like graphene and bulk diamond[23-25]. However, the related theoretical research about fluorinated diamane is deficient, especially on mechanical failure mechanism, carrier mobility and Raman spectra.

In this work, first-principle calculations were conducted on fluorinated diamane (denoted as FD hereafter) and hydrogenated diamane (namely HD hereafter) material. It was revealed that their elastic moduli are comparable to that of graphene. By combining the deformation potential theory and G_0W_0 method, we found that the relatively small effective mass plus high elastic modulus lead to high electron mobility and hole mobility in these two diamond-like monolayer materials, which is comparable or even better than that of bulk III-IV semiconductor compounds in consideration of their wide bandgap. Besides, we carefully explore the ideal strength and phonon instability to check the failure mechanism under applied biaxial and uniaxial strains. It is further identified that the tensile

[a] College of Chemistry and Molecular Engineering, Center for Nanochemistry, Academy for Advanced Interdisciplinary Studies, Peking University, Beijing 100871, China.
[b] State Key Laboratory for Structural Chemistry of Unstable and Stable Species, Beijing National Laboratory for Molecular Sciences, Peking University, Beijing 100871, China.
[c] Beijing Graphene Institute, Beijing 100095, China. E-mail: LiuZhiRong@pku.edu.cn
Electronic Supplementary Information (ESI) available: See DOI: 10.1039/x0xx00000x

strength of FD is dictated by soft-mode phonon instability under uniaxial strain and elastic instability under biaxial strain. The electronic properties can be further adjusted by external strains and fluorine vacancy defects. Finally, the predicted Raman spectrum is calculated to serve as a simple fingerprint to monitor the high-quality of diamane samples.

2 Method

2.1 Intrinsic carrier mobility under phonon scattering

The intrinsic carrier mobility of a high-quality sample is generally limited by the acoustic phonons at finite temperatures based on the widely used deformation potential theory[26-27]. This theory has been previously extended to the study of 2D materials[28-31], giving the same order of magnitude compared with the experimental results[29, 31]. Here for the 2D isotropic material, the mobility formula can be given as[30]:

$$\mu_x = \frac{e\hbar^3 C_{11}}{k_B T E_1^2 (m^*)^2} \quad (1)$$

where the C_{11} and m^* is the isotropic elastic constant (related with mechanical properties) and effective mass of charge carriers (electrons and holes) along the in-plane direction (related with the properties of electronic structure), E_1 is the deformation potential constant defined as the variation of the band-edge energy under the uniaxial strain $E_1 = \frac{\partial E_{edge}}{\partial \varepsilon}$(related with the electronic structure under different strains). T is the temperature with T = 298K being used in our study. Therefore, according to the Eq. (1), the carrier mobility of a material is both determined by the electronic and mechanical properties.

2.2 First-principle calculations

The calculations of geometric optimizations and electronic structures were based on the density functional theory (DFT) as implemented in the Vienna ab initio simulation package (VASP)[32]. The method of project augmented wave (PAW) pseudopotential was adopted to treat the interactions of electrons and ions cores[33]. To include the exchange-correlation function, the generalized gradient approximation (GGA) with the Perdew-Burke-Ernzerhof (PBE) method was used[34]. To correct the bandgap, the quasiparticle GW approach was performed on top of the PBE functional[35]. A total of 640 bands were used to ensure the E_g convergence to within 0.01eV. To be mentioned, the G_0W_0 approach can be sensitive to the initial starting DFT point, whereas self-consistent GW method could be a good choice as an alternative benchmark which imposing self-consistency to remove the starting point dependence[36-37]. However, this method is computationally expensive and not be performed in our calculations. A plane-wave cutoff of 500 eV and 15 × 15 × 1 k-point grid were chosen. Interlayer interactions were limited by setting spacing about 15 Å. The structures were fully relaxed until the residual forces were less than 0.01eV/Å. For the phonon frequencies and vibration modes, the convergence criterion for the total energy and atomic forces was further set to 10^{-9} Ry and 10^{-5}Ry/au within the density functional perturbation theory (DFPT) method as implemented in Quantum Espresso package[38]. The stress-strain

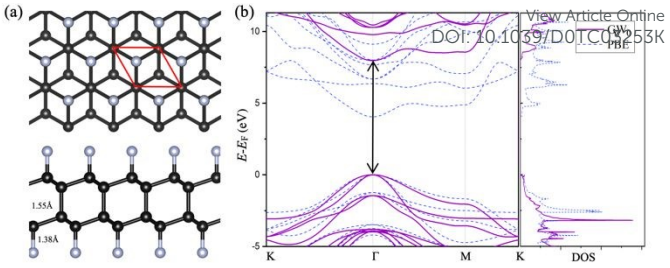

Figure 1. (a) Top and side views of FD with carbon (fluorine) atoms coloured in black (blue). Red rhombus denotes the unit cell. (b) Band structure and density of states of FD by using PBE (dashed) and G_0W_0 (solid) methods. The conduction band minimum (CBM) and valence band maximum (VBM) are pointed by the black arrow. Fermi level is set to at 0 eV.

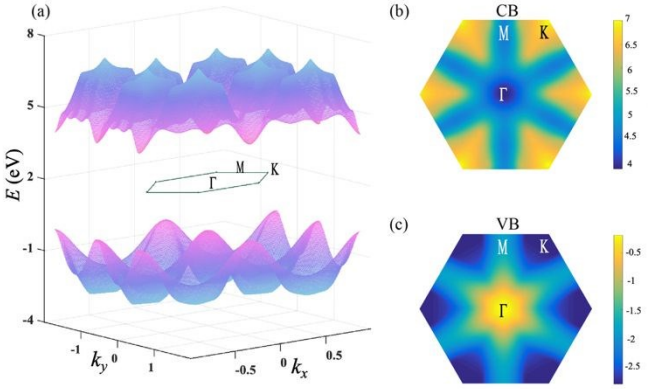

Figure 2. (a) 3D band structure of FD by using PBE method. (b, c) The band projection in the first Brillouin zone for the (b) CBM and (c) VBM.

calculations are performed in the orthogonal unit cell and the in-plane cell stress was rescaled by Z/d_0 to obtain the equivalent stress similar to previous literatures about graphene and MoS_2 [23, 39], where Z is the length of the cell along z axis and d_0 is the thickness of diamane plus the van der Waals distance. The above parameter settings were obtained on the basis of a series of tests for the energy convergence with respect to the energy cutoff, the thickness of the vacuum layer, the k-point mesh and the force convergence (**Figure S1 and S2**). The calculation results showed that the used parameter in our calculations can provide enough accuracy and allow reproducibility.

3 Results and discussion

3.1 Geometric and electronic structures

Figure 1a illustrates the top and side views of fluorinated AB-stacked diamane. Compared with another widely studied diamane, HD, the major difference is the terminated edge on both sides. The optimized in-plane lattice constant is 2.56 Å (2.53 Å) for FD (HD), while the C-C bond length is about 1.55 Å (1.56 Å) and the C-F (C-H) bond length is around 1.38 Å (1.11 Å), agreeing well with the recently reported experiment for FD and calculations for both[21, 40-41]. They are also close to the lattice constant of (111) surface of bulk diamond (2.52 Å)[13]. The band structure and density of states for FD by PBE and G_0W_0 method are depicted in **Figure 1b**. They look similar to the conduction band minimum (CBM) and the valence band maximum (VBM) at the Γ point, giving a bandgap about 4.04 and 7.96 eV,

View Article Online
DOI: 10.1039/D0TC03257K

respectively, indicating its direct-wide gap electronic properties. Specially, two bands are doubly degenerated at the VBM. Similar to FD, HD also shows a direct bandgap characteristic but with a lower value of about 3.32 eV (4.10 eV) in PBE (G_0W_0) method (**Figure S3**). **Figure 2a** shows the three-dimensional plots of the highest valence band (VB) and the lowest conduction band (CB). Apparently, Γ (K) point locates in the highest (lowest) of VB and the lowest (highest) of CB from the band projection in the first Brillouin zone (**Figure 2b, c**), further verifying its features of the direct bandgap, which appeals to applications in ultraviolet optics.

3.2 Mechanical properties and carrier mobility

Despite the wide bandgap for FD, FD possesses a large curvature at the CBM in **Figure 1b**, indicating its relatively small effective mass of conduction electrons. Moreover, carbon materials such as graphene and bulk diamond usually have superhigh mechanical strength[2, 13]. These two factors may together contribute to an extraordinary carrier mobility according to the Eq. (1). Thence, we further investigated the mechanical properties and carrier mobility at room temperature in FD as well as HD materials. The in-plane elastic constant *C* could be obtained by the total energy variation in first-principle calculations under strain, and derived other elastic properties by the following relationships[42]: $G = C_{66}, Y = (C_{11}C_{22} - C_{12}^2)/C_{22}$. The determined elastic constants, effective mass, deformation potential constant, and carrier mobility are summarized in **Table 1** (detailed determination of the deformation potential constant E_1 are shown in **Figure S4**). To further check the reliability of the effective mass, we calculated the effective masses of the highest valence band and doubly degenerated lowest conduction band using both G_0W_0 and PBE methods as shown in **Table S1**, and found no much differences between two methods.

The in-plane Young's modulus *Y* represents the rigidity of a material. As shown in **Table 1**, the values of FD (480 J/m^2) and HD (459 J/m^2) are close to (and slightly lower than) that of graphene (340.3 J/m^2) considering the thickness difference. Besides, the shear modulus *G* (217 and 226 J/m^2 for FD and HD, respectively) is also comparable to that graphene (144 J/m^2) under shear strain[28, 31]. All these elastic moduli are higher than most other 2D materials, indicating the outstanding mechanical properties in the diamane materials, which are similar to graphene and bulk diamond.

Table 1. Determined elastic modulus (in-plane elastic constant C_{11}, shear modulus *G* and Young's modulus *Y*), effective mass m^*, deformation potential constant E_1 and hole (electron) mobility μ at VBM (CBM) for FD and HD at 298 K. The m_e is the electron mass. The VBM is doubly degenerated at Γ, giving two values for hole carriers.

System	Elastic modulus			VBM (hole)			CBM (electron)		
	C_{11} (J/m^2)	G (J/m^2)	Y (J/m^2)	$m^*(m_e)$	E_1 (eV)	μ(cm^2 V^{-1}s^{-1})	m^* (m_e)	E_1 (eV)	μ(cm^2 V^{-1}s^{-1})
FD	485	217	480	1.13/ 0.37	–4.75/ –10.05	356/ 743	0.55	–3.59	2732
HD	490	226	459	0.58/ 0.21	–4.41/ –12.37	1565/ 1505	1.11	–3.97	536

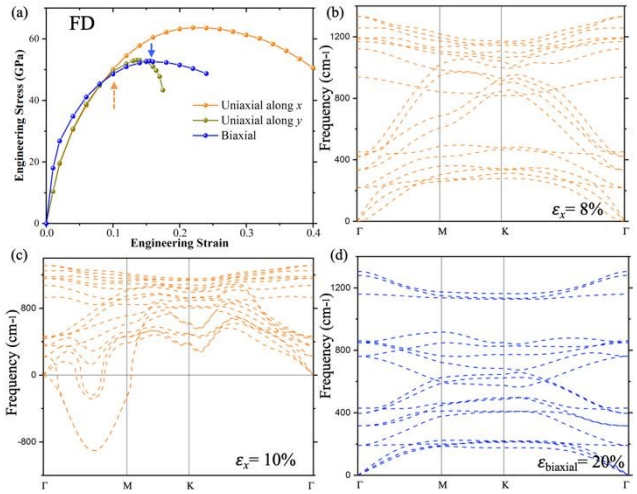

Figure 3. (a) Calculated ideal tensile stress versus engineering strain for single-layer FD. The solid and dash arrows represent the strains for phonon instability and elastic instability, respectively. (b-d) Calculated phonon dispersion under (b) uniaxial strain along the *x* direction with ε_x = 8%, (c) uniaxial strain along the *x* direction with ε_x = 10% and (d) biaxial strain with $\varepsilon_{biaxial}$ = 20%.

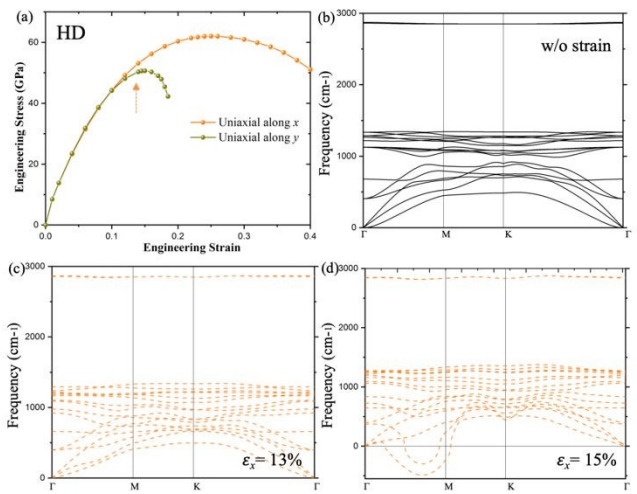

Figure 4. (a) Calculated ideal tensile stress versus engineering strain for single-layer HD. The solid and dash arrows represent the strains for phonon instability. (b-d) Calculated phonon dispersion (b) without strain, under (c) uniaxial strain along the x direction with ε_x = 13% and under (c) uniaxial strain along the x direction with ε_x = 15%.

Figure 3 shows the calculated ideal tensile stress-strain relations and phonon dispersions for single layer FD under both uniaxial and biaxial strain conditions. The curves in **Figure 3a** are nearly degenerated along the two orthogonal directions at small uniaxial strains, indicating that FD is an isotropic 2D material. As the strain increases, the stress-strain behaviours become nonlinear and show much difference between *x* and *y* directions. Their critical strains under elastic instability for these two directions locate at 22% (ideal strength is 63.6 GPa) and 13.5% (ideal strength is 53.07 GPa), respectively. However, we should also consider the phonon instability here, by further examining the conditions of phonon dispersion, as shown in **Figure 3b-d.** At the uniaxial strain ε_x = 10%, three acoustic phonon branches, and one optical branch have imaginary frequencies [**Figure 3c**]. In other words, the failure mechanism for FD under uniaxial tension along the *x* direction becomes phonon instability with a critical strain of 8%. In contrast to uniaxial strains, the phonon dispersion has no imaginary frequency under biaxial strain when reaches the maximum critical strain of 15.5%, indicating the failure mechanism of elastic instability.

For the single layer HD, the calculated ideal tensile stress-strain relations and phonon dispersions are shown in **Figure 4**. Similar to FD, the isotropic characteristic is verified by the nearly same values under small uniaxial strain along the *x* and *y* direction and presents difference when the applied strain increases. The calculated ideal strength is 63.64 GPa at the critical tensile strain ε_x = 25% and 51.94 GPa at critical tensile strain ε_y = 15%. We further examine the phonon frequencies, the calculated phonon dispersion for HD under strain-free state is shown in **Figure 4b**. It can be seen that all the phonon modes remain stable at the uniaxial strain ε_x = 13% (**Figure 4c**), but when ε_x = 15%, one of three acoustic branches correspond to vibration out of the plane (ZA) become unstable, as shown in **Figure 4d**.

We then further calculated the carrier mobility at room temperature in FD and HD materials. Carrier mobility usually drops dramatically with increasing the bandgap, e.g., the data for bulk III-IV semiconductor compounds are well described by a reverse law of $\mu \propto E_g^{-3/2}$[43]. However, as shown in **Table 1**, the small effective mass

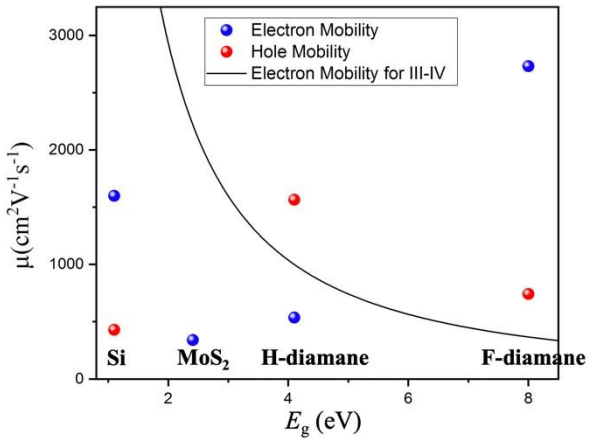

Figure 5. The correlation between carrier mobility μ and bandgap E_g for FD and HD, with bulk III-IV semiconductor compounds (solid line, described by $\mu = 0.83 \times 10^4 \times Eg^{-3/2}$ in ref.[40]), monolayer MoS_2 and bulk Si (data from ref.[41]) as comparisons. The calculated data for electron/hole mobility are plotted in red/blue symbols.

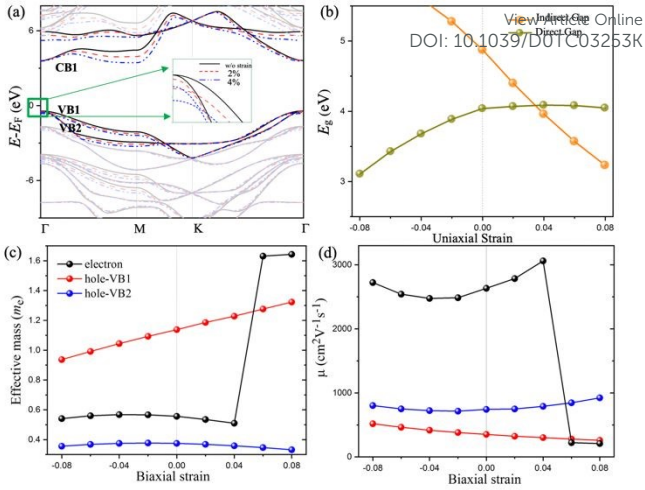

Figure 6. (a) Strain effects on the electronic band structure of FD by using PBE method. Inset: Enlarged band structure inside the green box. The VB1 and VB2 are used to mark the doubly degenerated VBM. The CBM are marked by CB1. The black solid line is the unstrained system and the red dotted (blue double dotted) line is the band structure under 2% (4%) uniaxial tensile strain. (b) The bandgap E_g as a function of the applied uniaxial strain. The direct bandgap at Γ point under different strain is shown in green symbol, while the indirect bandgap from Γ to M is shown in orange symbol.

of carrier, high elastic modulus, and moderate deformation potential constant, contribute to the extraordinary electron mobility in FD and hole mobility in HD. In our study, the calculated electron mobility in FD is as high as 2732 $cm^2V^{-1}s^{-1}$, about seven times larger than that of the bulk III-IV semiconductor compounds if extrapolating them to the same bandgap (**Figure 5**). It is about one order of magnitude larger than that in MoS_2 films[44]. The doubly degenerated band at the VBM in FD and HD gives here the hole mobility with two branches, as presented in **Table 1**. The branch with a larger value for FD is also a little superior over the bulk III-IV semiconductor. Specially, the smaller effective mass of hole in HD endows its much higher hole mobility of about 1565 $cm^2V^{-1}s^{-1}$, which are competitive with bulk silicon (e.g., 450 $cm^2V^{-1}s^{-1}$)[44], offering attractive alternatives to conventional semiconductors in the electronic applications.

3.3 Electronic properties modulated by strain and defects

Given the promising performances and successfully prepared in experiments for FD, we investigated the influence of the applied strain and the common vacancy defects of materials on the electronic properties of FD. We applied −8%~8% (increment of 2%) strain to the FD, and the electronic band structures of FD under no strain, 2% and 4% uniaxial tensile strain by using PBE method are presented in **Figure 6a**. It can be clearly seen that the doubly degenerated VBM at Γ could separate into two branches under the strain from the enlarged inset in **Figure 6a**. More specially, we found that the CB1 gradually fall at M as the stretching strain increases and becomes lower than Γ when the strain exceeds 2.7%, changing the direct bandgap (green symbols in **Figure 6b**) in FD to an indirect one from Γ to M (orange symbols in **Figure 6b**). In contrast, the direct bandgap characteristics is maintained under the compressed strain. In addition, the resulting real bandgaps of FD was modulated to decrease no matter under stretching or compressed strain, which are

View Article Online
DOI: 10.1039/D0TC03257K

expected to improve the carrier mobility for the potential application.

To verify our guess, we explored the bandgap, effective mass and carrier mobility with respect to the applied biaxial strain (-8%~8%), as shown in **Figure 6c-d** and **Figure S5**. The bandgap also decreases under the compressed strain and undergoes a transition from direct to indirect from Γ to M under the stretching biaxial strain similar to the uniaxial strain, but here the critical strain is 5% (**Figure S5**). In addition, the effective mass of FD can be controlled by applying the biaxial strain. The hole carrier effective mass (VB1) depends linearly on the biaxial strain, for example, it drops from 1.13 m_0 to 0.92 m_0 by applying biaxial strains of 0% (unstrained) and -8%, respectively. Meanwhile, the hole mobility for VB1 branch increases from 356 to 518 $cm^2V^{-1}s^{-1}$ by about 1.5 times. For the electron carrier effective mass (CB), it linearly decreases form 0.55 m_0 to 0.50 m_0 under the stretching biaxial strain of 4%, causing the electron mobility increasing from 2732 to 3061 $cm^2V^{-1}s^{-1}$, but experiences a fluctuation as strain increases, this may be caused by the CBM jumping from Γ to M point during the bandgap transition from direct to indirect at a strain of 5%. Most interestingly, at M point, the deformation potential constant (E_{1x}(M)=-5.4 and E_{1y}(M)=-21.8) and effective mass (m^*_x(M)=0.19, m^*_y(M)=14.0 m_0 for a biaxial strain of 6%, m^*_x(M)=0.20, m^*_y(M)=13.5 m_0 for a biaxial strain of 8%, we plot $\sqrt{(m^*_x \times m^*_y)}$ in **Figure 6c** for the comparison) is anisotropic in contrast to Γ and K point, which keeps the six-fold symmetry. At this time, the electron mobility along the *x* direction will be related with both the value of *x* and *y* direction[30], therefore abruptly jumps to 222 and 210 $cm^2V^{-1}s^{-1}$ with an applied biaxial strain of 6% and 8%, respectively.

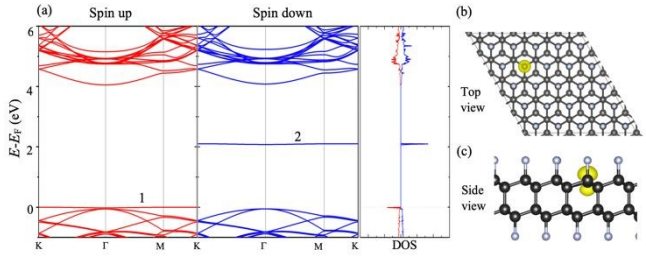

Figure 7. (a) Spin-polarized band structure and density of states of FD 5×5 supercell with a single fluorine vacancy (V_F) by using PBE method. The localized defect states are labeled as 1 and 2. (b) The top view and (c) the side view of Γ point wave functions of the states 1and 2 in (a). Fermi level is set to at 0 eV.

Another potential modulation method is to introduce defects. Vacancy defects are actually inevitable in real experiments. For example, fluorine vacancy defect (V_F) was observed and found to have an obvious influence on the transport and optical properties for FD[21]. **Figure 7a** shows the spin-polarized band structure and density of states of 5×5 supercell FD with a single V_F. The presence of the V_F introduces the localized defect states (labelled as 1 and 2) in the bandgap and leads to a transition from direct 7.96 eV to indirect 4.00 eV bandgap by using the G_0W_0 method, which greatly reduces the bandgap. Moreover, levels of 1 and 2 are donor and acceptor states, respectively. Both of them seem to act as deep level and maybe have no doping effect for the material because the acceptor level is far away from VBM and the donor level is away from CBM. Therein, other dopants such as nitrogen or boron element may be a better candidate to realize *n*-type or *p*-type carriers here, which has been previously raised in bulk diamond[13]. According to the wave functions of states 1 and 2 at the Γ point, as shown in the top view and side view in **Figure 7b, c**, the defect level originates from the p_z orbital of C atom around V_F. Besides, to see how the V_F affects the carrier mobility, we also calculated the elastic modulus, effective mass and deformation potential constant under such situation (**Figure S6**). Although the defect states are within the bandgap, we found that the elastic modulus (482 J/m^2) and effective mass (0.34, 1.11 and 0.54 m_0 for VB2, VB1 and CB, respectively) almost unchanged compared to non-defect state, and the deformation potential constant (for VB2, VB1 and CB at Γ point is -8.72, -5.13 and 3.60 eV, respectively) changed a little. Therefore, the electron mobility is 2732 $cm^2V^{-1}s^{-1}$, and hole mobility for two degenerated branches is 317 and 1103 $cm^2V^{-1}s^{-1}$ with V_F defects.

3.3 Raman characterization

Raman scattering spectroscopy is one of the most popular characterization tool for 2D materials due to its convenient, rapid and non-destructive characteristics[45]. To give an easy fingerprint for experimentally obtained high-quality FD, we further theoretically investigated the Raman spectrum, which has been applied in other new 2D materials and compared with experiments[46-47]. Here for FD, Γ-point phonons could be represented by the irreducible representations of D_{3d} as: $\Gamma = 3A_{1g} + 2A_{2u} + 2E_u + 3E_g$, where one A_{2u} and one E_u are acoustic modes, the other A_{2u} and E_u are infrared active, and the A_{1g}, E_g are Raman active. Here, "*E*" denotes the doubly degenerate modes in *xy*-plane, and A_{1g} as the breathing modes shown in **Figure 8a.** The typical vibrational modes of Raman-active phonons and the predicted Raman scattering spectra of FD are exhibited in **Figure 8b.** The predicted frequencies of the Raman modes in FD are 1174 (A^1_{1g}), 1279 (E_g), and 1338 (A^2_{1g}) cm^{-1}, which could be remarkably distinguished from graphene (about 1580 cm^{-1} in G band), HD (about 1345 and 2886 cm^{-1}) and bulk diamond (main peak is about 1333 cm^{-1})[48-50]. In addition, the A_{1g} and E_g modes of FD can be both observed in the usual backscattering configuration according to the Raman tensors of vibrational modes, which will be convenient for 2D sheets.

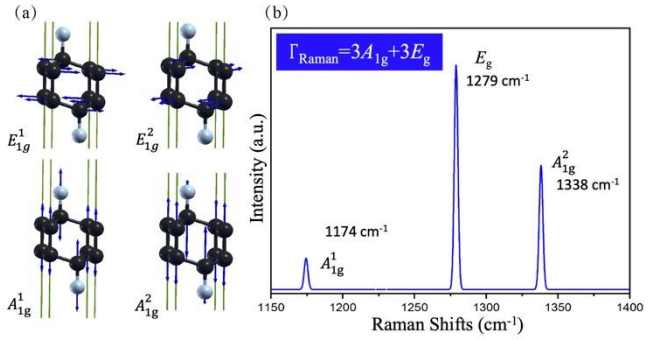

Figure 8. (a) The atomic displacements of four Raman-active vibrational modes in FD with a unit cell. (b) The predicted Raman spectra of FD. Inset: Irreducible representations of Γ point Raman-active phonons. The frequencies of presented Raman modes in (a) are labelled in (b).

Conclusions

In summary, we have systematically explored the electrical and mechanical properties of fluorinated single layer diamond (FD) as well as hydrogenated single layer diamond (HD) inspired by the recently successful grown of the large-area fluorinated diamond monolayer by chemical vapor deposition approach. Combining the G_0W_0 method with a three-dimensional band structure, we found that FD is a direct-wide bandgap material of 7.96 eV at Γ point, with doubly degenerated bands at the valence band maximum (VBM), leading to two branches for the hole mobility. These characteristics are similar to HD, except the bandgap of HD is lower with 4.10 eV using the G_0W_0 method. Their mechanical strengths are found to comparable to graphene with Young's modulus 480 and 459 J/m^2 for FD and HD, respectively, which are more superior over most known 2D materials. We further explore the ideal strength and failure mechanism including elastic and phonon instability under applied biaxial and uniaxial strains. It is identified that the tensile strength of FD is dictated by soft-mode phonon instability under critical uniaxial strain ε_x = 8% and elastic instability under critical biaxial strain $\varepsilon_{biaxial}$ = 15.5%, while for HD, the critical uniaxial strain is ε_x = 13% due to the failure mechanism of phonon instability. Moreover, the surprising large curvature at the conduction band maximum (CBM) in FD and VBM in HD indicates that the relatively small effective mass of conduction electrons and valence holes. Both excellent elastic modulus plus small effective mass lead to the electron mobility of about 2732 $cm^2V^{-1}s^{-1}$ in FD, and the hole mobility of about 1565 $cm^2V^{-1}s^{-1}$ in HD, much larger than bulk silicon and MoS_2, also competitive with traditional III-IV semiconductor materials considering the wide bandgap. Such electronic properties could also be modulated with decreasing the bandgap by the means of applied strain or fluorine vacancy (V_F), especially a bandgap transition that was found from direct to indirect at the case of tensile strain upon 2.7%. We also give a simple fingerprint in theory, that is, the Raman-active phonons frequencies of FD to help to experimentally check the high-quality of FD samples. We expect that these two diamond-like materials have great potential for future applications in nano-optics and nanoelectronics, and could also serve as a promising platform for nano-electromechanical systems.

Conflicts of interest

There are no conflicts to declare.

Acknowledgements

The authors thank Prof. Feng Ding for helpful suggestions. The authors acknowledge financial support from the National Natural Science Foundation of China (Grant No. 21773002) and Beijing National Laboratory for Molecular Sciences (BNLMS-CXTD-202001). The work was supported by High-performance Computing Platform of Peking University.

Notes and references

1 Balandin, A. A.; Ghosh, S.; Bao, W., *et al.*, Superior thermal conductivity of single-layer graphene. *Nano Lett.* 2008, **8**, 902-907.
2 Lee, C.; Wei, X.; Kysar, J. W., *et al.*, Measurement of the elastic properties and intrinsic strength of monolayer graphene. *Science* 2008, **321**, 385-388.
3 Novoselov, K. S.; Geim, A. K.; Morozov, S. V., *et al.*, Two-dimensional gas of massless Dirac fermions in graphene. *Nature* 2005, **438**, 197-200.
4 Zhang, Y. B.; Tan, Y. W.; Stormer, H. L., *et al.*, Experimental observation of the quantum Hall effect and Berry's phase in graphene. *Nature* 2005, **438**, 201-204.
5 Butler, S. Z.; Hollen, S. M.; Cao, L., *et al.*, Progress, Challenges, and Opportunities in Two-Dimensional Materials Beyond Graphene. *ACS Nano* 2013, **7**, 2898-2926.
6 Gong, C.; Zhang, X., Two-dimensional magnetic crystals and emergent heterostructure devices. *Science* 2019, **363**, 706.
7 Wang, Q. H.; Kalantar-Zadeh, K.; Kis, A., *et al.*, Electronics and optoelectronics of two-dimensional transition metal dichalcogenides. *Nat. Nanotechnol.* 2012, **7**, 699-712.
8 Huang, M.; Bakharev, P. V.; Wang, Z.-J., *et al.*, Large-area single-crystal AB-bilayer and ABA-trilayer graphene grown on a Cu/Ni(111) foil. *Nat. Nanotechnol.* 2020, **15**, 289-295.
9 Huang, M.; Biswal, M.; Park, H. J., *et al.*, Highly Oriented Monolayer Graphene Grown on a Cu/Ni(111) Alloy Foil. *ACS Nano* 2018, **12**, 6117-6127.
10 Wu, T.; Zhang, X.; Yuan, Q., *et al.*, Fast growth of inch-sized single-crystalline graphene from a controlled single nucleus on Cu-Ni alloys. *Nat. Mater.* 2016, **15**, 43-47.
11 Xu, X.; Zhang, Z.; Dong, J., *et al.*, Ultrafast epitaxial growth of metre-sized single-crystal graphene on industrial Cu foil. *Sci. Bull.* 2017, **62**, 1074-1080.
12 May, P. W., Diamond thin films: a 21st-century material. *Philos. Trans. R. Soc. London, Ser. A* 2000, **358**, 473-495.
13 Wort, C. J. H.; Balmer, R. S., Diamond as an electronic material. *Mater. Today* 2008, **11**, 22-28.
14 Gao, Y.; Cao, T.; Cellini, F., *et al.*, Ultrahard carbon film from epitaxial two-layer graphene. *Nat. Nanotechnol.* 2018, **13**, 133-138.
15 Odkhuu, D.; Shin, D.; Ruoff, R. S., *et al.*, Conversion of multilayer graphene into continuous ultrathin sp(3)-bonded carbon films on metal surfaces. *Sci. Rep.* 2013, **3**, 3276.
16 Rajasekaran, S.; Abild-Pedersen, F.; Ogasawara, H., *et al.*, Interlayer carbon bond formation induced by hydrogen adsorption in few-layer supported graphene. *Phys. Rev. Lett.* 2013, **111**, 085503.
17 Chernozatonskii, L. A.; Sorokin, P. B.; Kvashnin, A. G., *et al.*, Diamond-like C2H nanolayer, diamane: Simulation of the structure and properties. *JETP Lett.* 2009, **90**, 134-138.
18 Kvashnin, A. G.; Chernozatonskii, L. A.; Yakobson, B. I., *et al.*, Phase diagram of quasi-two-dimensional carbon, from graphene to diamond. *Nano Lett.* 2014, **14**, 676-81.
19 Liu, C.; Xu, X.; Qiu, L., *et al.*, Kinetic modulation of graphene growth by fluorine through spatially confined decomposition of metal fluorides. *Nat. Chem.* 2019, **11**, 730-736.
20 Xie, Y.; Cheng, T.; Liu, C., *et al.*, Ultrafast Catalyst-Free Graphene Growth on Glass Assisted by Local Fluorine Supply. *ACS Nano* 2019, **13**, 10272-10278.
21 Bakharev, P. V.; Huang, M.; Saxena, M., *et al.*, Chemically induced transformation of chemical vapour deposition grown bilayer graphene into fluorinated single-layer diamond. *Nat. Nanotechnol.* 2019, **15**, 59-66.
22 Mostafa Raeisi, B. M., Evgeny V. Podryabinkin, Fazel Shojaei, Xiaoying Zhuang, Alexander V. Shapeev, High thermal conductivity in semiconducting Janus and non-Janus diamanes. *Carbon* 2020, **167**, 51-61.

23 Liu, F.; Ming, P.; Li, J., Ab initio calculation of ideal strength and phonon instability of graphene under tension. *Phys. Rev. B* 2007, **76**, 064120.
24 Nie, A.; Bu, Y.; Li, P.*, et al.*, Approaching diamond's theoretical elasticity and strength limits. *Nat. Commun.* 2019, **10**, 5533.
25 Banerjee, A.; Bernoulli, D.; Zhang, H.*, et al.*, Ultralarge elastic deformation of nanoscale diamond. *Science* 2018, **360**, 300-302.
26 Bardeen, J.; Shockley, W., Deformation potentials and mobilities in non-polar crystals. *Phys. Rev.* 1950, **80**, 72-80.
27 Herring, C.; Vogt, E., Transport and deformation potential theory for many-valley semiconductor with anisotroic scattering. *Phys. Rev.* 1956, **101**, 944-961.
28 Cheng, T.; Lang, H.; Li, Z.*, et al.*, Anisotropic carrier mobility in two-dimensional materials with tilted Dirac cones: theory and application. *Phys. Chem. Chem. Phys.* 2017, **19**, 23942-23950.
29 Fischetti, M. V.; Laux, S. E., Band structure, deformation potentals, and carrier mobility in strained Si, Ge, and SiGe alloys. *J. Appl. Phys.* 1996, **80**, 2234-2252.
30 Lang, H.; Zhang, S.; Liu, Z., Mobility anisotropy of two-dimensional semiconductors. *Phys. Rev. B* 2016, **94**, 235306.
31 Li, Z.; Wang, J.; Liu, Z., Intrinsic carrier mobility of Dirac cones: The limitations of deformation potential theory. *J. Chem. Phys.* 2014, **141**.
32 Kresse, G.; Furthmuller, J., Efficient iterative schemes for ab initio total-energy calculations using a plane-wave basis set. *Phys. Rev. B* 1996, **54**, 11169-11186.
33 Kresse, G.; Joubert, D., From ultrasoft pseudopotentials to the projector augmented-wave method. *Phys. Rev. B* 1999, **59**, 1758-1775.
34 Perdew, J. P.; Burke, K.; Ernzerhof, M., Generalized gradient approximation made simple. *Phys. Rev. Lett.* 1996, **77**, 3865-3868.
35 Hybertsen, M. S.; Louie, S. G., Electron correlation in semiconductors and insulators-bandgaps and Quasi-particel energies. *Phys. Rev. B* 1986, **34**, 5390-5413.
36 Foster, M. E.; Wong, B. M., Nonempirically Tuned Range-Separated DFT Accurately Predicts Both Fundamental and Excitation Gaps in DNA and RNA Nucleobases. *J. Chem. Theory Comput.* 2012, **8**, 2682-2687.
37 Kaplan, F.; Harding, M. E.; Seiler, C.*, et al.*, Quasi-Particle Self-Consistent GW for Molecules. *J. Chem. Theory Comput.* 2016, **12**, 2528-2541.
38 Giannozzi, P.; Baroni, S.; Bonini, N.*, et al.*, QUANTUM ESPRESSO: a modular and open-source software project for quantum simulations of materials. *J. Phys.-Condes. Matter* 2009, **21**, 395502.
39 Li, T., Ideal strength and phonon instability in single-layer MoS2. *Phys. Rev. B* 2012, **85**, 235407.
40 Zhu, L.; Zhang, T., Suppressed thermal conductivity in fluorinated diamane: Optical phonon dominant thermal transport. *Appl. Phys. Lett.* 2019, **115**, 151904.
41 Zhu, L.; Hu, H.; Chen, Q.*, et al.*, Formation and electronic properties of hydrogenated few layer graphene. *Nanotechnology* 2011, **22**, 185202.
42 Wei, Q.; Peng, X., Superior mechanical flexibility of phosphorene and few-layer black phosphorus. *Appl. Phys. Lett.* 2014, **104**, 251915.
43 Wang, J.; Zhao, R.; Yang, M.*, et al.*, Inverse relationship between carrier mobility and bandgap in graphene. *J. Chem. Phys.* 2013, **138**, 084701.
44 Intrinsic transport properties of electrons and holes in monolayer transition-metal dichalcogenides. *Phys. Rev. B* 2014, **90**, 045422.
45 Zhang, S.; Zhang, N.; Zhao, Y.*, et al.*, Spotting the differences in two-dimensional materials - the Raman scattering perspective. *Chem. Soc. Rev.* 2018, **47**, 3217-3240.
46 Zhang, S.; Wang, J.; Li, Z.*, et al.*, Raman Spectra and Corresponding Strain Effects in Graphyne and Graphdiyne. *J. Phys. Chem. C* 2016, **120**, 10605-10613.
47 Cheng, T.; Tan, C.; Zhang, S.*, et al.*, Raman Spectra and Strain Effects in Bismuth Oxychalcogenides. *J. Phys. Chem. C* 2018, **122**, 19970-19980.
48 Pimenta Martins, L. G.; Matos, M. J. S.; Paschoal, A. R.*, et al.*, Raman evidence for pressure-induced formation of diamondene. *Nat. Commun.* 2017, **8**, 96.
49 Ferrari, A. C.; Meyer, J. C.; Scardaci, V.*, et al.*, Raman spectrum of graphene and graphene layers. *Phys. Rev. Lett.* 2006, **97**, 187401.
50 Liyan Zhu, F. D., Giant thermal conductivity in diamane and the influence of horizontal reflection symmetry on phonon scattering. *Nanoscale* 2019, **11**, 4248-4257.

View Article Online
DOI: 10.1039/D0TC03253K